



Synchrotron x-ray total scattering and modeling study of high-pressure-induced inhomogeneous atom reconfiguration in an equiatomic $Zr_{50}Cu_{50}$ metallic glassy alloy

Shifeng Luo ^{1,2,3}, Jia Chuan Khong,^{2,4} Dominik Daisenberger,⁵ Shi Huang,² Paul F. McMillan,⁶ and Jiawei Mi ^{2,7,*}

¹*School of Materials Science and Engineering, Hefei University of Technology, Hefei 230009, Anhui, People's Republic of China*

²*Department of Engineering, University of Hull, Cottingham Road, Hull HU6 7RX, United Kingdom*


³*State Key Laboratory of Solidification Processing, School of Materials Science and Engineering, Northwestern Polytechnical University, Xi'an 710072, People's Republic of China*

⁴*Department of Medical Physics & Biomedical Engineering, University College London, London WC1E 6BT, United Kingdom*

⁵*Diamond Light Source Ltd., Harwell Campus, Didcot OX11 0DE, United Kingdom*

⁶*Department of Chemistry, University College London, London WC1H 0AJ, United Kingdom*

⁷*School of Materials Science and Engineering, Shanghai Jiao Tong University, Shanghai 200240, People's Republic of China*

 (Received 20 July 2021; revised 11 January 2022; accepted 18 January 2022; published 10 February 2022)

We studied *in situ* the local atomic structure evolution of an equiatomic $Zr_{50}Cu_{50}$ metallic glassy alloy under high pressure compression inside a diamond anvil cell using synchrotron x-ray total scattering. The empirical potential structure refinement method was used to reconstruct the three-dimensional atomic models at each pressure step, and to analyze the spatially averaged local atomic structure configurations. The interatomic distances of different atomic pairs are reduced at different rates with increasing pressure and the Cu-Cu pairs exhibit the highest percentage reduction. Between ambient pressure and 36.85 GPa, the atomic separation of the Cu-Cu pairs is reduced by $\sim 12\%$ compared to $\sim 5\%$ for Zr-Zr and Zr-Cu pairs. Such disproportional decrease in interatomic distance results in inhomogeneous atom reconfiguration in the short atomic range. With the increase of pressure, the Zr atoms move preferentially towards the Zr-Zr pairs, while the Cu atoms move preferentially towards the Cu-Cu pairs, creating inhomogeneous atom reconfiguration with positive short-range order coefficients of 0.0309 and 0.0464 for Zr-Zr and Cu-Cu respectively, but a negative value of -0.0464 for Zr-Cu pairs. Voronoi tessellation method was also used to study the evolution of the short-range atom packing versus pressure, elucidating the cause for the bimodal distribution of the bond angle distributions. The research sheds light on understanding of the atomic reconfiguration of equiatomic alloys under high pressure.

DOI: [10.1103/PhysRevB.105.064203](https://doi.org/10.1103/PhysRevB.105.064203)

I. INTRODUCTION

Metallic glasses (MGs) often have very high elastic limit, fracture strength, and exceptional corrosion/wear resistance due to their disordered atomic structures [1–3]. In the long atomic range (>20 Å), the disordered atom arrangement is generally viewed as a homogeneous structure. However, local structure heterogeneities do exist in the short atomic range (<5 Å) and medium atomic range (5–20 Å), forming the so-called short-range ordered (SRO) or medium range ordered (MRO) atomic structures [4,5]. They determine, to a certain degree, the properties of MGs with the same composition but different processing histories [6,7]. Thus one of the important research directions in MGs is to control or tune the atomic structures so as to enhance the desired functionality and property. In this aspect, understanding precisely the 3D local atomic structures and their changes under different thermodynamic conditions is absolutely necessary.

Pressure is an important thermodynamic driving force to govern or control the atomic structures of a material. As the

density increases with pressure, a polyamorphic transition has been found to occur in a number of MG systems, i.e., a sudden change from a low-density amorphous state (LDA) to a high-density amorphous state (HDA). In recent years, pressure-dependent atomic structures and elastic property changes in MGs have been widely reported [8–22] and have become an important research direction in the condensed-matter physics community. For the MG systems that do not exhibit any polyamorphic transition under compression, their densities increase monotonically with pressure [8–11], and the corresponding decrease in atomic volume can be well described by bulk modulus and its pressure derivative obtained by fitting a Birch-Murnaghan equation of state [23,24]. However, such an approach can only describe the macroscopic volume change versus pressure; it does not give any specific information about changes in the local atomic structure during compression, for instance, how different atomic species move in three-dimensional (3D) space to accommodate the increase in pressure.

For MG systems that do exhibit a distinct pressure-induced polyamorphic transition [12–22], most reports so far have concentrated on studying the change of electronic structures in order to elucidate and understand the origin of polyamorphism. For example, in the $Ce_{55}Al_{45}$ alloy, two distinct

*Corresponding author: j.mi@hull.ac.uk

amorphous states with different densities were observed [12]; *ab initio* molecular dynamics modeling and x-ray absorption spectroscopy revealed that such the phenomenon is associated with delocalization of the $4f$ electron and bond shortening [12,14]. A similar polyamorphic transition reported in the Ca-Al MG system is caused by the pressure-enhanced bonding between Ca $3d$ and Al $3p$ orbitals [20,22]. Until now, only a few reports are found in the open literature describing the evolution of 3D atomic structure under high pressure [25,26]. Systematic studies between atomic structure and pressure for most MG systems have not been seen reported, e.g., we do not know how different atoms move or reconfigure and how they interact with each other in 3D space in order to adapt or accommodate the increase of pressure. In addition, although polyamorphic transition has been observed and reported in some MG systems with one dominant principal element (e.g., lanthanide based [12–18], main-group based [20,22], and transition metal based [21]), high-pressure-induced local atomic structure changes in equiatomic alloys have not been reported so far. However, alloy design with equiatomic ratio for all principal alloy elements is a central concept of high-entropy alloys. The research reported in this paper provides understanding on the local atomic structure evolution of an equiatomic MG under high pressure compression.

An equiatomic metallic glass ($Zr_{50}Cu_{50}$) was chosen as the experimental alloy in this work because the Zr-Cu system can be used to make bulk amorphous alloys over a wide compositional range from 50 to 66 at. % Cu [27,28]. These materials exhibit a wide range of useful mechanical properties including shape-memory effects combined with high hardness and toughness [29,30]. Numerous studies on the local atomic structure have been made by molecular dynamics modeling and synchrotron x-ray diffraction or neutron diffraction experiments [31–34], which can provide us with reliable structure data for comparison. For example, at the $Zr_{50}Cu_{50}$ composition the atomic packing fraction within the MG alloy is approximately 3.2% lower than that of its crystalline counterpart estimated from MD simulations [31], consistent with the large proportion of icosahedral and other non-fully-close packed polyhedral units involved in the local atomic arrangements. Mattern reported that many different polyhedra are observed in $Zr_{50}Cu_{50}$ metallic glass, and no dominant structural arrangement exists [33]. However, those studies just focused on the atomic structure at ambient pressure.

In this work, we used synchrotron x-ray total scattering (SXTS) to study *in situ* the atomic structure evolution of an equiatomic glassy alloy ($Zr_{50}Cu_{50}$) in a diamond anvil cell up to 36.85 GPa. The empirical potential structure refinement (EPSR) modeling method [35] was used to reconstruct the 3D atomic structure at each pressure level. By analyzing the decoupled partial pair distribution functions (PDFs) and interrogating the local 3D atomic structures at each pressure level, the atomic reconfiguration and rearrangement as a function of pressure is elucidated and quantified. We focus on studying the changes of local coordination and revealing the trend towards inhomogeneous atom reconfiguration in the Zr-centered and Cu-centered coordination polyhedra. Our study elucidates the underlying changes in coordination environment that can lead to inhomogeneous atom reconfiguration driven by high pressure in equiatomic metallic glasses, an

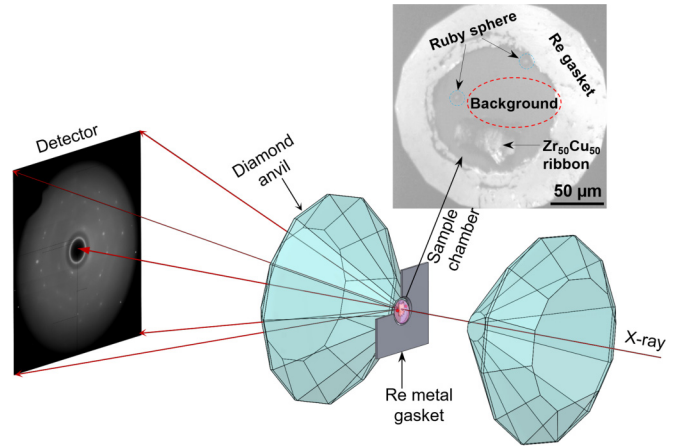


FIG. 1. A schematic of the experimental setup of the *in situ* SXTS experiments under high pressure carried out at I15 of DLS, with an optical image showing the $Zr_{50}Cu_{50}$ sample and the ruby sphere (as pressure calibrant) inside the sample chamber.

important phenomenon which has been largely ignored in most previous high pressure studies.

II. MATERIALS AND METHODS

A. Preparation of $Zr_{50}Cu_{50}$ metallic glassy alloy

The $Zr_{50}Cu_{50}$ glassy alloy was prepared by melting pure Zr and Cu elemental button ingots (each with a purity >99.9%) inside an arc remelting furnace under the Ti-gettered argon atmosphere. The alloy was remelted at least four times to ensure chemistry homogeneity before melt-spin into ribbons with a thickness of $\sim 30 \mu\text{m}$ using a single-roller melt-spinning method. The ribbon sample was cut into $\sim 50\text{-}\mu\text{m}$ pieces using tungsten carbide tweezers.

B. *In situ* SXTS experiments under high pressure

In situ SXTS experiments under high pressure were carried out at the I15 beamline of Diamond Light Source (DLS), UK. Figure 1 shows the schematic of the experimental setup and the diamond anvil cell (DAC) used to produce quasi-hydrostatic high pressures. The two diamond anvils were held by two Tungsten carbide backing plates. A rhenium (Re) gasket $250 \mu\text{m}$ thick with a small hole ($\sim 150 \mu\text{m}$ diameter) in the middle was used to form the sample chamber, and 4:1 methanol:ethanol was used as the pressure transmission medium. The pressure was measured by an iHR320 spectrometer using the ruby fluorescence method. The positions of the sample and ruby sphere are shown in the inset in Fig. 1. The high pressures inside the DAC sample chamber were achieved by increasing the membrane pressure using the gas pressure controller mounted outside the experiment hutch. In this work, the maximum pressure of 36.85 GPa was achieved inside the DAC sample chamber.

During *in situ* SXTS experiments, a monochromatic x-ray beam (energy: 72 keV; spot size: $\sim 70 \mu\text{m}$ diameter) and a Perkin Elmer flat panel 1621 EN detector (image size: 2048×2048 pixels; pixel size: $200 \times 200 \mu\text{m}^2$) were used to collect the SXTS patterns at each pressure step. Detector calibration

was carried out using a NIST silicon standard at a sample-to-detector distance of 327.638 mm. Five scattering patterns (exposure time of 120 s for each pattern) were acquired and summed for the sample and background at each pressure step to ensure a sufficient signal-to-noise ratio for the data collection. A long exposure time was selected because of the combination of (1) amorphous sample, (2) small sample size (only $\sim 30 \mu\text{m}$ thick), (3) the small x-ray beam size ($\sim 70 \mu\text{m}$ diameter), and (4) the x-ray absorption and relatively high scattering background by the DAC. The background scattering patterns were acquired by moving the sample away and allowing the incident x-ray beam to pass through the empty area within the sample chamber.

C. SXTS at ambient pressure

To compare the SXTS of the sample at ambient pressure without DAC, additional measurement was acquired using the same detector (Perkin Elmer 1621 EN), with an x-ray energy of 76 keV. Compared to the SXTS experiments with DAC at high pressure, only 10 s exposure was collected as there was no absorption of x ray by DAC. NIST standard CeO_2 powder was used to calibrate the detector (sample-to-detector distance of 265.885 mm). Again, five scattering patterns were acquired and summed for sample and background.

D. Data processing

For the scattering data acquired under high pressure, the Bragg spots due to the DAC were removed from the 2D scattering patterns using a MATLAB script as shown in Appendix 1 (see Fig. S1) of the Supplemental Material [36]. Then the atomic density, structure factor, $S(Q)$, and PDF, $g(r)$, at different pressures were calculated using an iterative procedure (MATLAB script in Appendix 2) as described in detail in the Supplemental Material [36] (see, also, Refs. [37–47] therein). For comparison, the atomic density of the sample at ambient pressure was also calculated using the iterative procedure, but the 2D scattering patterns were not processed by the MATLAB script in Appendix 1 since there were no Bragg spots on the 2D scattering patterns acquired at ambient pressure.

In this work, $Q_{\text{max}} = 9.25 \text{ \AA}^{-1}$ was used to calculate $S(Q)$ and $g(r)$ at each pressure step. As the calculated atomic densities were quite stable in the Q_{max} range of 8.75 to 9.25 \AA^{-1} (Fig. S2b), the atomic density, background factor, and r_{min} were averaged by the results obtained at $Q_{\text{max}} = 8.75, 9.00$, and 9.25 \AA^{-1} to improve the accuracy of results.

III. EPSR MODELING

The EPSR method (EPSR version 25) [35] was used in this work to reconstruct the 3D atomic structures and to extract the partial PDFs from the total PDFs at each pressure step. The total potential energy (U) of the system used in EPSR consists of a reference potential (U^{Ref}) and an empirical potential (U^{EP}) as below:

$$U = U^{\text{Ref}} + U^{\text{EP}}. \quad (1)$$

TABLE I. Lennard-Jones potential parameters of Zr and Cu atoms used in EPSR modelling [48].

Atoms	ε (kJ/mol)	σ (Å)	q
Zr	0.609 61	3.1993	0
Cu	0.338 07	2.5487	0

For an atomic pair i - j , the potential energy between them is described as

$$U_{ij}(r) = U_{ij}^{\text{Ref}}(r) + U_{ij}^{\text{EP}}(r), \quad (2)$$

where i and j represent the atoms (i.e., Zr and Cu atoms in this work), and r is the distance between atom i and atom j . The total potential energy of the system is calculated by

$$U = \frac{1}{2} \sum_i \sum_j U_{ij}(r_{ij}). \quad (3)$$

First, the reference potential is a Lennard-Jones 12-6 potential plus effective Coulomb charges as below:

$$U_{ij}^{\text{Ref}}(r) = 4\varepsilon_{ij} \left[\left(\frac{\sigma_{ij}}{r} \right)^{12} - \left(\frac{\sigma_{ij}}{r} \right)^6 \right] + \frac{q_i q_j}{4\pi \varepsilon_0 r}, \quad (4)$$

$$\varepsilon_{ij} = \sqrt{\varepsilon_i \varepsilon_j}, \quad (5)$$

$$\sigma_{ij} = \frac{1}{2}(\sigma_i + \sigma_j), \quad (6)$$

where ε_{ij} and σ_{ij} are the well depth parameter and range parameter of atomic pair i - j respectively. q_i and q_j are the charges of atom i and atom j respectively, and ε_0 is the vacuum permittivity.

Table I lists the parameters for the Zr and Cu atom used in the model to calculate the reference potential of the $\text{Zr}_{50}\text{Cu}_{50}$ system. In the simulation, after the modeled system reaches the equilibrium state driven by the reference potential alone, the peak positions of the EPSR modeled $S(Q)$ and $g(r)$ are compared to the corresponding $S(Q)$ and $g(r)$ obtained from the SXTS. If the difference is larger than a predefined value, then the Lennard-Jones parameters (ε and σ) need to be modified until the simulated results agree with the experimental data.

Second, the empirical potential energy is refined. Generally, it is not the “12-6” type formula as the reference potential. A series of power exponential functions are used to refine the empirical potential [35],

$$U_{ij}^{\text{EP}} = kT \sum_i C_i P_{n_i}(r, \sigma_r), \quad (7)$$

$$P_n(r, \sigma) = \frac{1}{4\pi \rho \sigma^3 (n+2)!} \left(\frac{r}{\sigma} \right) \exp \left[-\frac{r}{\sigma} \right], \quad (8)$$

where C_i are positive or negative real, and σ_r is a width function.

In each iteration, a R factor is used to access the difference between the simulated $S(Q)$ and experimental $S(Q)$. For example, if the R factor $> 10^{-3}$, then a refined feedback is given to recalculate and refine the empirical potential until the R factor $< 10^{-3}$ is reached. Then the simulation results are considered to match the experimental ones. In this work,

the refined empirical potential of 11 kJ/mol was used in the simulation.

Finally, after refining the empirical potential, ~ 2500 calculation cycles are made and the results are accumulated to obtain an averaged statistical information in the simulation box, such as partial PDFs, coordination numbers. The procedures for how to run EPSR modeling can be found in the manual [35].

Coordination numbers of the atomic pair (N_{ij}) in the first atomic shell are calculated from the corresponding partial PDF $g_{ij}(r)$ by Eq. (7),

$$N_{ij} = 4\pi c_j \int_0^{r_{\max}} g_{ij}(r) r^2 dr, \quad (9)$$

where c_j is the mole fraction of atom j , and r_{\max} is the upper limit of integration. Generally, r_{\max} is set to the upper limit of the interatomic distance of each atomic pair in the first atomic shell. In this work, the cutoffs of 4.0, 3.7, and 3.5 Å are used for Zr-Zr, Zr-Cu, and Cu-Cu atomic pairs respectively. Then the coordination numbers around the i th atom (N_i) and the average coordination number (N) can be calculated from N_{ij} using Eqs. (8) and (9),

$$N_i = N_{ii} + N_{ij}, \quad (10)$$

$$N = c_i N_i + c_j N_j, \quad (11)$$

where i and j represent the alloy elements (Zr and Cu).

In this work, a cubic simulation box containing a total of 5000 atoms (2500 Zr atoms and 2500 Cu atoms) was used. The simulation was carried out in one of the dedicated computing nodes [2×14 -core Broadwell E5-2680v4 processors (2.4–3.3 GHz), 128 GB DDR4 RAM] of Hull University supercomputing cluster, Viper. Normally, it takes approximately 6 h computing time (~ 2500 iterations) to complete a typical simulation with a satisfactory R factor $< 10^{-3}$. At each pressure step, three identical simulations are done to gain sufficient statistical data and reproducibility. The results presented in this work are the averaged values of the three simulations.

IV. RESULTS

A. *In situ* SXTS results

The average atomic density of the sample at different pressures is determined from the x-ray total scattering data using an iterative method [46] (see the Supplemental Material [36]). At ambient pressure, it is 55.9×10^{-3} atoms/Å³, only 2% lower than a previously reported bulk value (57.1×10^{-3} atoms/Å³) for Zr₅₀Cu₅₀ metallic glass [33]. Figure 2(a) shows that the atomic density increases with the increase of pressure, and no abrupt change is found during the pressure up. The x-ray scattering intensities $I(Q)$ at different pressures are shown in Fig. 2(b) for the Q range 0.2–6.0 Å⁻¹. As the pressure increases, the first peak shifts from 2.7 to 2.9 Å⁻¹. There is no obvious change in the relative intensities of the first and second peaks of $I(Q)$ that might associate with polymorphic transitions as reported previously for different alloys [16,17]. Between ambient pressure and 36.85 GPa, the

first peak shifts almost linearly from 2.7074 to 2.8494 Å⁻¹ (5% increase). The corresponding $S(Q)$ calculated from $I(Q)$ using the iterative procedure are shown in Fig. 2(c). Similarly, all $S(Q)$ curves show the similar profiles, with the first peak position moving towards higher Q as the pressure increases, indicating that the average interatomic separations decrease with the increase of pressure. While the relatively unchanged intensities for the first and second peak indicates that no polymorphic transformation occurs. By Fourier transformation, the PDFs, $g(r)$, are shown in Fig. 2(d). As expected, the first peak in $g(r)$ peak decreases from 2.885 Å at ambient pressure to 2.723 Å at 36.85 GPa, consistent with overall densification of the MG structure.

B. EPSR modeling results

The 3D atomic structure model is reconstructed using the EPSR modeled results [35] (Video 1 shows more vividly the 3D atomic configurations when zooming into the r range near the third, second, and first atomic shells). The simulated $S(Q)$ and $g(r)$ agree well the SXTS results [Figs. 2(c) and 2(d)]. A typical atomic configuration of the sample at ambient pressure reconstructed by EPSR modeling is shown in Fig. 2(e). Based on the reconstructed atomic structure, the partial $S(Q)$ s of the Zr-Zr, Zr-Cu, and Cu-Cu atomic pairs at different pressures are extracted [Figs. 3(a)–3(c)]. And the relationships between the total $S(Q)$ and the three partial $S(Q)$ s at ambient pressure and 36.85 GPa are shown in Fig. S3 [36]. With increasing the pressure, the first peak position in all three pairs moves towards higher Q . To obtain the information in real space, the partial PDFs are calculated [Figs. 3(d)–3(f)]. All three partial PDFs shift towards lower r with the increase of pressure, and the Cu-Cu pair separation is shortened the most [the insets in Figs. 3(g) and 3(h)]. As the $g(r)$ s move to lower r , the peak heights of the first peak of $g_{\text{Zr-Zr}}(r)$ and $g_{\text{Cu-Cu}}(r)$ increase with the increase of pressure, and the Cu-Cu pair has the largest percentage increase with $\sim 38.6\%$. However, those for the $g_{\text{Zr-Cu}}(r)$ remain relatively unchanged [Figs. 3(i) and 3(j)]. Furthermore, the full width at half maximum (FWHM) of the first peak in $g_{\text{Zr-Zr}}(r)$ and $g_{\text{Cu-Cu}}(r)$ decreases monotonously as the pressure increases [Figs. 3(k) and 3(l)], indicating that a progressive inhomogeneous atom reconfiguration occurs. While that of the first peak in $g_{\text{Zr-Cu}}(r)$ varies randomly [Figs. 3(k) and 3(l)]. For comparison, the FWHM of the first peak in $g(r)$ is also calculated and overlapped in Figs. 3(k) and 3(l). It remains unchanged in the whole pressure range, which may be attributed to the fact that the Q_{\max} used to perform Fourier transformation is really small, and thus the subtle inhomogeneous atom reconfiguration cannot be detected by the change in FWHM of $g(r)$ [49].

The SXTS results give globally averaged information over all coordination environments for the atoms presented in the system. Based on the modeled partial PDFs, we extract the average first shell coordination number information around each atom specie (i.e., Zr and Cu in this case) at each pressure step (Fig. S4 [36]). Both N_{ZrZr} and N_{CuCu} have a higher percentage of increase with pressure. N_{ZrZr} increases by 14.8% and N_{CuCu} by 10.5% at 36.85 GPa, respectively, while N_{ZrCu} and N_{CuZr} remain unchanged and should be equal because of the equimolar concentration of both elements in the sample.

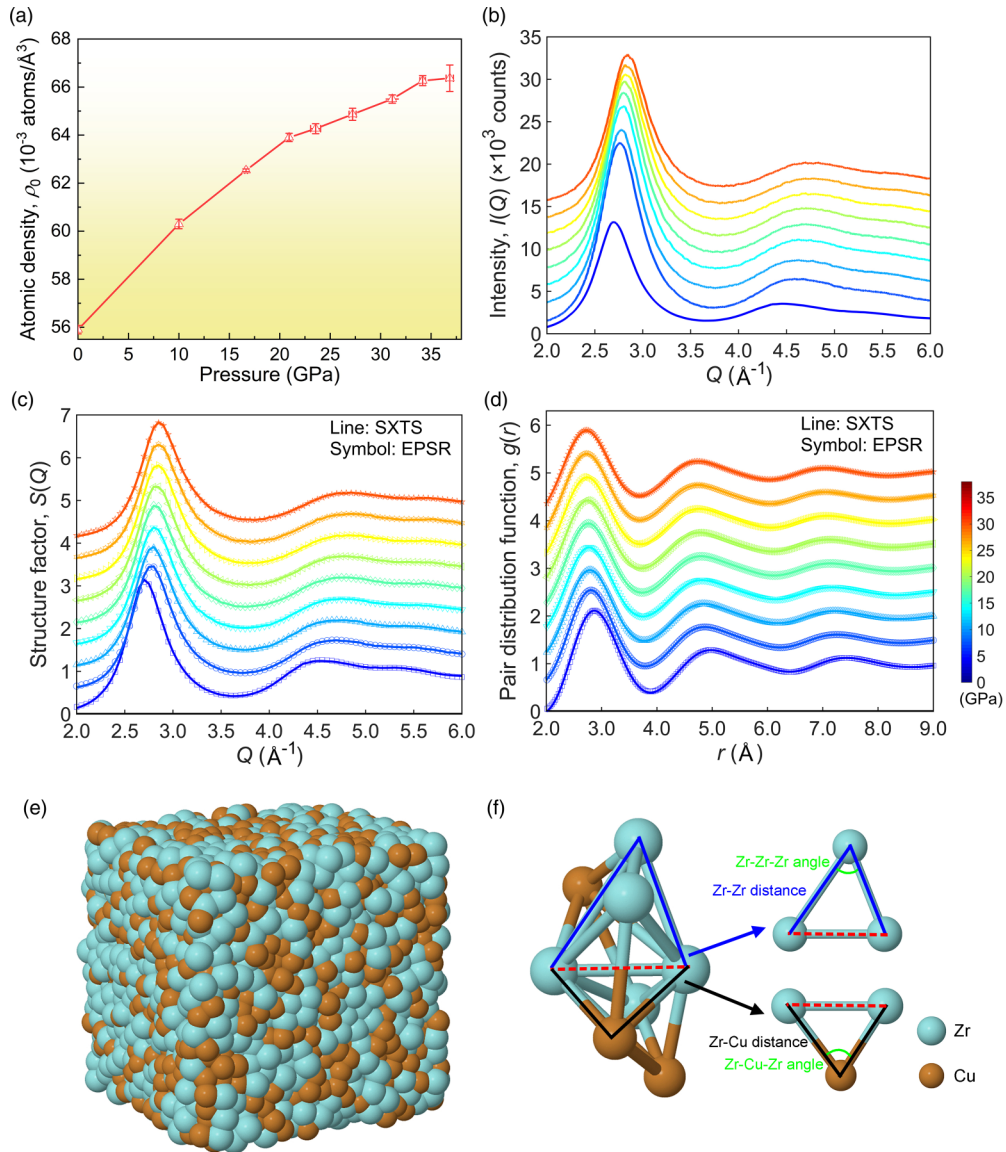


FIG. 2. The ρ_0 , $I(Q)$, $S(Q)$, and $g(r)$ curves obtained from the SXTS data using the iterative procedure as well as the simulated $S(Q)$ and $g(r)$ curves by EPSR modeling at each pressure step and a 3D atomic configuration. (a) The ρ_0 of sample as a function of pressure, (b) the $I(Q)$ curves. (c) Experimental $S(Q)$ curves and the EPSR simulated results. (d) Experimental $g(r)$ curves and the EPSR simulated results. Note: the vertical error bars in Fig. 2(a) indicate the accuracy of atomic density determined using the iterative procedure. (e) The atomic configuration of Zr₅₀Cu₅₀ metallic glassy alloy reconstructed by EPSR modeling at ambient pressure. (f) An example showing the local 3D atomic configuration in direct contact with the selected Zr-Zr pair. Note the 100% van der Waals radius is used in Fig. 2(e), while 25% van der Waals radius is used in Fig. 2(f) to present the 3D atomic structures more clearly.

In addition, N_{Zr} and N_{Cu} have a relatively lower percentage of increase with pressure. N_{Zr} is larger than N_{Cu} at all pressures, reflecting the size effect of the atoms [33]. Based on the coordination number information, the chemical ordering averaged over the local coordination environments can be quantified by the short-range order coefficient (η_{ij}^0) proposed by Cargill and Spaepen [50],

$$\eta_{ij}^0 = \left(\frac{N_{ij}N}{c_j N_i N_j} - 1 \right) / \eta_{ij}^{\text{max}}. \quad (12)$$

Here $\eta_{ij}^{\text{max}} = c_j N_j / (c_i N_i)$ for $c_j N_j < c_i N_i$ and $\eta_{ij}^{\text{max}} = c_i N_i / (c_j N_j)$ for $c_j N_j > c_i N_i$. While $\eta_{ij}^0 = 0$ represents a full

chemically disordered system, $\eta_{ij}^0 = 1$ for a full chemically ordered arrangement. $\eta_{ij}^0 > 0$ means that j th atoms prefer to distribute around i th atoms, while $\eta_{ij}^0 < 0$ indicates that j th atoms are not likely to aggregate towards i th atoms. Figure 4(a) shows the η^0 of each atomic pair as a function of pressure. At ambient pressure, η^0 of Zr-Zr, Cu-Cu, and Zr-Cu pairs are -0.0095 , -0.0137 , 0.0137 and respectively, much smaller than the values (0.05, 0.07, and -0.06 respectively) reported for bulk amorphous Zr₅₀Cu₅₀ metallic glass [33], indicating that the alloy is in an almost fully chemically disordered state [see the schematic of atomic configurations on the left of Fig. 4(a)]. With the increase of pressure, η^0 of

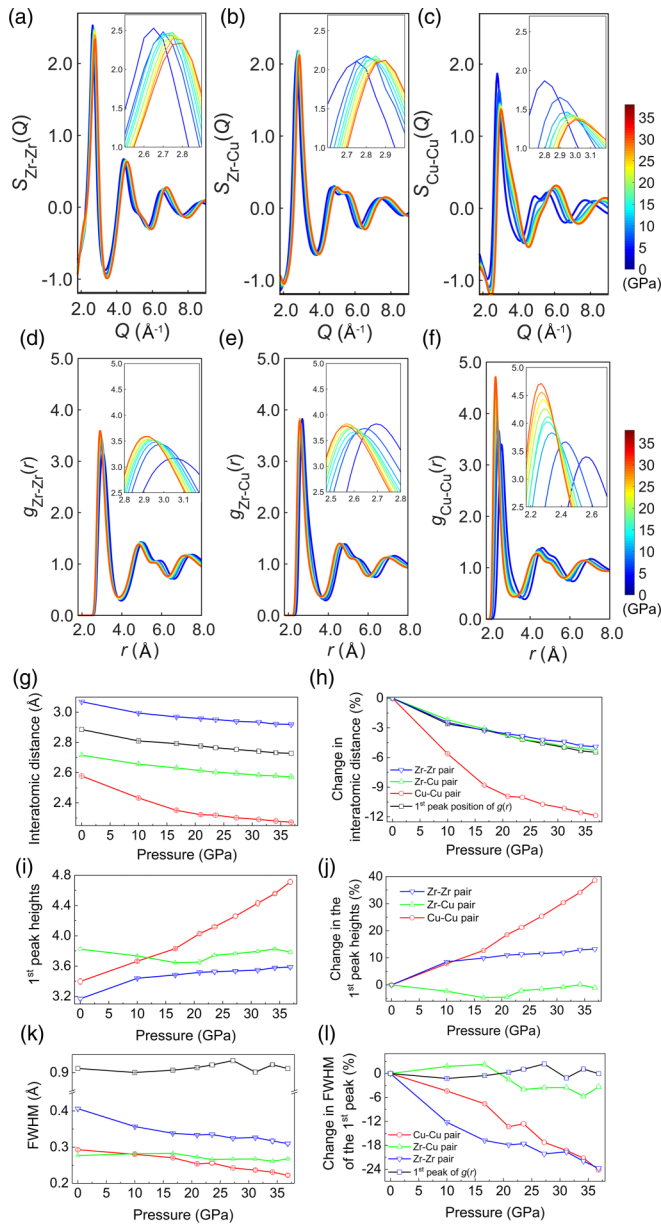


FIG. 3. Changes in the first peak of three partial PDFs at different pressure steps. (a)–(c) The partial $S(Q)$ s of Zr-Zr, Zr-Cu, and Cu-Cu pairs with the insets showing the shifts of positions and heights of the first peak respectively. (d)–(f) The partial PDFs of Zr-Zr, Zr-Cu, and Cu-Cu pairs with the insets showing the shifts of positions and heights of the first peak respectively. (g), (h) The interatomic distances of three atomic pairs and their relative changes at different pressures respectively. For comparison, the first peak position in $g(r)$ curves and its relative change are also plotted. (i), (j) The first peak heights of the three atomic pairs and their relative changes at different pressures. (k), (l) The full width at half maximum (FWHM) of the first peak of the three atomic pairs and their relative changes at different pressures respectively. For comparison, the FWHM of the first peak in $g(r)$ curves and its relative change are also plotted.

the like-atom pairs (i.e., Zr-Zr and Cu-Cu pairs) increases monotonically, while that of the unlike-atom pairs (i.e., Zr-Cu and Cu-Zr pairs) decreases [see the schematic of atomic configurations on the right of Fig. 4(a)].

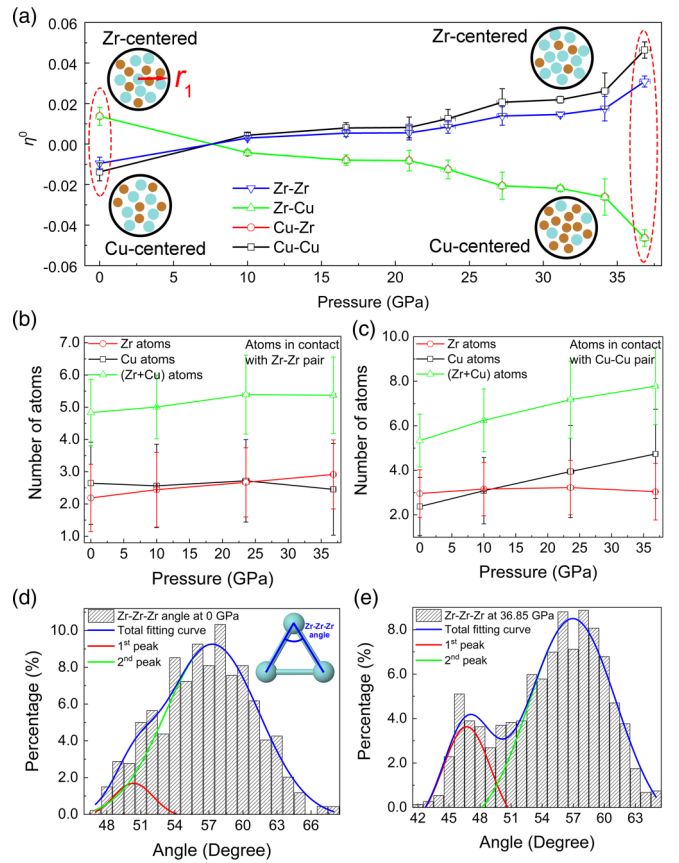


FIG. 4. The short-range order coefficient η^0 and the local 3D atomic structures information extracted from EPSR model. (a) η^0 as a function of pressure for four atomic pairs. The insets highlight the local 3D atomic configurations at the selected pressure. (b), (c) The number of atoms that are in direct contact with Zr-Zr and Cu-Cu pairs respectively. Note that the interatomic distances of Zr-Zr and Cu-Cu pairs within $\pm 0.1\%$ of the peak positions in the partial PDFs are extracted. (d), (e) The bond angle distributions of Zr-Zr-Zr linkage at ambient pressure and 36.85 GPa respectively with an inset in (d) highlighting the Zr-Zr-Zr linkage extracted from the local 3D atomic structure. The fitting results of determining the two peaks by fitting two Gaussian functions are also plotted.

To understand how the Zr and Cu atoms rearrange themselves as the pressure increases, the configuration of atoms in contact with the Zr-Zr/Cu-Cu pair is extracted from the EPSR model [see Fig. 2(f)], where the interatomic distances of each selected Zr-Zr/Cu-Cu pair are within $\pm 0.1\%$ of the peak positions in the partial PDFs [Figs. 3(d) and 3(f)]. The results from four pressure steps are selected to illustrate the trend. For the like-atom pairs, i.e., the Zr-Zr and Cu-Cu pairs, Fig. 4(b) shows that the number of the nearest neighbor Zr atoms in direct contact with the Zr-Zr pairs increases linearly with pressure. Figure 4(c) shows a similar trend for the nearest neighbor Cu atoms in direct contact with the Cu-Cu pairs. However, for the unlike-atom pair, i.e., the Zr-Cu pair, Fig. 4(b) shows that the number of the nearest neighbor Cu atoms in direct contact with the Zr-Zr pairs remains almost unchanged. Similarly, the number of the nearest neighbor Zr atoms in direct contact with the Cu-Cu pairs remains unchanged [Fig. 4(c)]. Similar calculations are made for the interatomic distances within

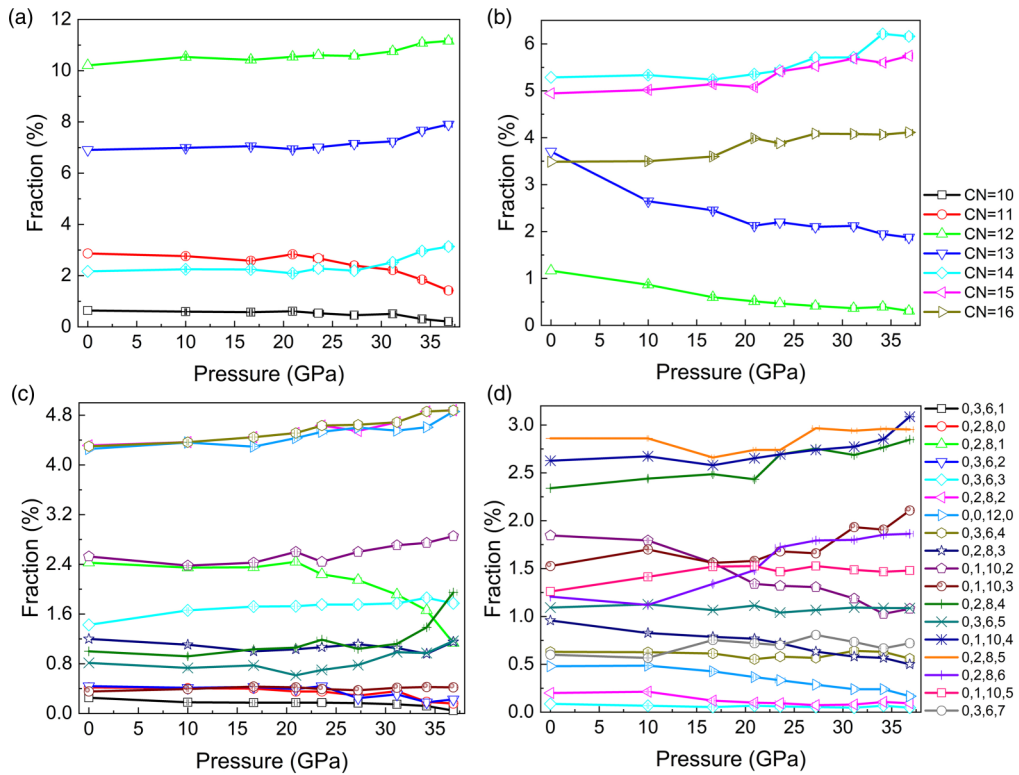


FIG. 5. Evolution of coordination number and Voronoi polyhedra (VPs) at different pressures. (a),(b) Cu- and Zr-centered VPs with different CNs as a function of pressure respectively. (c),(d) Some popular Cu- and Zr-centred VPs as a function of pressure.

$\pm 0.05\%$ and 0.2% of the peak position in the partial PDFs (see Fig. S5 [36]). The number of atoms in the different environments exhibits the same trends as shown Figs. 4(b) and 4(c). Such consistent results indicate that the number of the like-atom clusters increases with pressure. Furthermore, with increasing pressure, the near-Gaussian type bond angle distribution [Fig. 4(d)] for the Zr-Zr-Zr linkage separates into a bimodal type distribution with two peaks [Fig. 4(e)]. Similar trends are found in the Zr-Cu-Zr, Cu-Zr-Cu, and Cu-Cu-Cu linkages (see Fig. S6 [36]). Although the first peak in the other three linkages are more distinguishable than that of the Zr-Zr-Zr linkage at ambient pressure, the first peak become more obvious at high pressure.

The short-range atomic packing structures are further studied by the Voronoi tessellation method [51], and the coordination numbers (CNs) and Voronoi polyhedra (VPs) of the Cu-centered and Zr-centered local atomic structure were extracted and analyzed. Figures 5(a) and 5(b) show the fractions of CNs for Cu-centered and Zr-centered VPs. Clearly, for the Cu-centered VPs, the fraction of the VPs with CN = 12 is higher than others (i.e., CN = 11, 13, and 14), while for the Zr-centered VPs, those with CN = 14 and CN = 15 are higher than the others. This is due to the large radii of Zr atom. As the pressure increases, low-coordinated VPs transfer into high coordinated VPs for both cases, i.e., 10- and 11-coordinated VPs transfer into 12-, 13-, and 14-coordinated ones [Fig. 5(a)], and 12- and 13-coordinated VPs transfer into 14-, 15-, and 16-coordinated ones [Fig. 5(b)]. Figures 5(c) and 5(d) illustrate some popular VPs centered by Cu and Zr atoms respectively. The $\langle 0, 2, 8, 2 \rangle$, $\langle 0, 0, 12, 0 \rangle$, and $\langle 0, 3, 6, 4 \rangle$ VPs

with fractions over 4.1% are the higher ones in Cu-centered VPs [Fig. 5(c)], while $\langle 0, 2, 8, 4 \rangle$, $\langle 0, 1, 10, 4 \rangle$, and $\langle 0, 2, 8, 5 \rangle$ VPs are the higher ones in Zr-centered VPs [Fig. 5(d)]. With increasing pressure, fractions of Cu-centered $\langle 0, 2, 8, 0 \rangle$ and $\langle 0, 2, 8, 1 \rangle$ VPs decreases significantly, while those of $\langle 0, 2, 8, 2 \rangle$, $\langle 0, 0, 12, 0 \rangle$, $\langle 0, 3, 6, 3 \rangle$, $\langle 0, 3, 6, 4 \rangle$, $\langle 0, 1, 10, 2 \rangle$, and $\langle 0, 2, 8, 4 \rangle$ VPs increase. Similarly, in Zr-centered VPs, fractions of $\langle 0, 1, 10, 3 \rangle$, $\langle 0, 2, 8, 4 \rangle$, $\langle 0, 1, 10, 4 \rangle$, and $\langle 0, 2, 8, 6 \rangle$ VPs increase with the pressure, while those of $\langle 0, 0, 12, 0 \rangle$, $\langle 0, 2, 8, 3 \rangle$, and $\langle 0, 1, 10, 2 \rangle$ VPs decrease.

V. DISCUSSION

A. The dominant atomic pair to control the deformation under high pressure

Using EPSR modeling to reconstruct the 3D atomic models that match the total PDFs obtained from SXTS at different pressures, we decouple all partial PDFs from the total PDFs and are therefore able to study the local 3D atomic configurations. Figure 3(h) clearly shows that the atomic distance of the Cu-Cu pair is shortened the most with the increase of pressure, i.e., $\sim 12\%$ at 36.85 GPa, while the Zr-Zr and Zr-Cu pairs distance have a very similar trend in shortening with $\sim 5\%$ at 36.85 GPa. The trend is very similar to that of the first peak of $g(r)$. Such convincing evidence indicates that the Cu-Cu pairs play the dominant role in responding to the high pressure compression. It is worth mentioning that the results obtained in this work are different from that of the $Zr_{66.7}Cu_{33.3}$ MG reported in [25,26]. They demonstrated that the Zr-Zr pairs are strained preferentially to coordinate the compression,

while Cu-Cu and Cu-Zr pairs remain least affected by the pressure load. This difference is due to the compositions. In $Zr_{66.7}Cu_{33.3}$ MG, the number of Zr-Zr bonds is much more than that of Zr-Cu and Cu-Cu bonds, and hence the elasticity of this alloy should be mainly determined by the solvent-solvent pairs [52], i.e., Zr-Zr pairs. By contrast, the alloy used in this work has an equal number of Zr and Cu atoms, and thus the number of Zr-Zr bonds is equal to that of Cu-Cu bonds. In this case, the dominant factor influencing the deformation behavior during compression should be their respective atomic radii and the ability to move locally. The atomic radius of the Cu atom is $\sim 19.6\%$ smaller than that of the Zr atom [53], and therefore Cu atoms are easier to move their spatial location so as to coordinate the compressional stress. Hence, the interatomic distances of Cu-Cu pairs decrease much more than that of Zr-Zr and Zr-Cu pairs in the $Zr_{50}Cu_{50}$ MG alloy [Fig. 3(h)].

B. Atomic structure reconfiguration and inhomogeneous atom reconfiguration under high pressure

Figure 2(d) clearly shows that the nearest neighbor distances in $Zr_{50}Cu_{50}$ MG decrease during densification, indicating the changes of atomic structure occur. During the high pressure compression, all the interatomic distances of three atomic pairs decrease monotonically with the pressure [Figs. 3(g) and 3(h)], while the peak heights of the $g_{Zr-Zr}(r)$ and $g_{Cu-Cu}(r)$ increase [Figs. 3(i) and 3(j)] and the FWHM of the first peak decreases, reflecting a progressive increase in inhomogeneous atom reconfiguration during compression. An in-depth analysis in Fig. 4(a) clearly shows that the short-range order coefficient of Zr-Zr and Cu-Cu pairs increases with the pressure, while that of the Zr-Cu pair decreases monotonically. Furthermore, the local 3D atomic structures extracted from EPSR model at each pressure step [Fig. 2(f)] shows that the trend that the same type of atoms are grouping together [Figs. 4(b) and 4(c)]. Such information that is extracted from the atom pair interactions for all atoms in the simulation box is statistically convincing evidence to support the argument for inhomogeneous atom reconfiguration found in this research.

At ambient pressure, for the Cu-centered VPs, there are more icosahedral like VPs (i.e., $\langle 0, 2, 8, 2 \rangle$ and $\langle 0, 0, 12, 0 \rangle$) than others, while for the Zr-centered VPs there are more face-centered-cubic-like VPs (i.e., $\langle 0, 2, 8, 4 \rangle$, $\langle 0, 1, 10, 4 \rangle$, and $\langle 0, 2, 8, 5 \rangle$). The bond angle distributions exhibit a near-Gaussian type distribution ($\angle ACB$ in Fig. S7 [36]). As the pressure increases, the interatomic distance of Zr-Zr and Cu-Cu pairs decreases. The pressure forces the low-coordinated VPs around both Zr atoms and Cu atoms to transfer into high-coordinated VPs. As illustrated in Fig. S7, under a high pressure, atom D moves towards atoms A and B, shortening the distance between atom D and atom A, as well as that between atom D and atom B, creating a new angle (i.e. $\angle A'D'B'$). The intensity of $\angle A'D'B'$ [i.e., the first peak in Fig. 4(e)] increases with pressure due to monotonous decrease of the distance of Zr-Zr and/or Cu-Cu pairs. The fractions of icosahedral-like VPs ($\langle 0, 1, 10, 3 \rangle$, $\langle 0, 2, 8, 4 \rangle$, $\langle 0, 1, 10,$

4), and $\langle 0, 2, 8, 6 \rangle$) decrease with pressure, while that of face-centered-cubic-like VPs ($\langle 0, 0, 12, 0 \rangle$, $\langle 0, 2, 8, 3 \rangle$, and $\langle 0, 1, 10, 2 \rangle$) increase. In the Cu-centered VPs, the fractions of both icosahedral-like VPs ($\langle 0, 2, 8, 2 \rangle$, $\langle 0, 0, 12, 0 \rangle$, $\langle 0, 3, 6, 3 \rangle$, and $\langle 0, 1, 10, 2 \rangle$) and face-centered-cubic-like VPs ($\langle 0, 3, 6, 4 \rangle$ and $\langle 0, 2, 8, 4 \rangle$) increase with pressure. Therefore, the more obvious appearance of the first peak in bond angle distributions at higher pressure is due to the increased fraction of face-centered-cubic-like VPs [Figs. 4(d) and 4(e) and Fig. S6].

VI. CONCLUSIONS

In this work, we studied *in situ* the local atomic structure evolution of an equiatomic $Zr_{50}Cu_{50}$ metallic glassy alloy under high pressure compression by SXTS and EPSR modeling. The important findings of this research are as follows:

(1) In the short atomic range, high pressure compression results in disproportional decrease in the interatomic distance for the Zr-Zr, Cu-Cu, and Zr-Cu atomic pairs. From ambient pressure to 36.85 GPa, the Cu-Cu pairs' interatomic distances reduce by $\sim 12\%$ compared to $\sim 5\%$ for that of the Zr-Zr and Zr-Cu pairs.

(2) As pressure increases, the Zr atoms move preferentially towards the Zr-Zr pairs, while the Cu atoms move preferentially towards the Cu-Cu pairs, creating inhomogeneous atom reconfiguration with positive short-range order coefficient of 0.0309 and 0.0464 for the like-atom pairs Zr-Zr and Cu-Cu respectively, but a negative value of -0.0464 for the unlike-atom pair Zr-Cu.

(3) The number of icosahedral like VPs and face-centered-cubic-like VPs around Cu atoms increases with pressure. The number of face-centered-cubic-like VPs around Zr atoms increases, while that of icosahedral like VPs decrease. This increase in the number of face-centered-cubic-like VPs causes the intensification of the first peak in the bond angle distributions.

ACKNOWLEDGMENTS

We would like to acknowledge the synchrotron x-ray beam time awarded by Diamond Light Source (Experiments No. EE8858-1 and No. EE9902-1). We would like also to acknowledge the use of the Viper High Performance Computer at the University of Hull and its team for technical support. S.L. and S.H. also acknowledge the financial support from the China Scholarship Council for their Ph.D. study at the University of Hull.

The authors declare that there are no competing financial interests or personal relationships that could have appeared to influence the work reported in this paper.

J.M. and P.F.M. conceived the idea and won the synchrotron x-ray beam time. J.M., J.C.K., and D.D. conducted the *in situ* synchrotron x-ray total scattering experiments under high pressure compression. S.L. and S.H. analyzed the synchrotron x-ray scattering data, performed the EPSR modeling work, and led the writing of the manuscript. All authors contributed to the writing and discussion of the manuscript.

- [1] A. Inoue and A. Takeuchi, Recent development and application products of bulk glassy alloys, *Acta Mater.* **59**, 2243 (2011).
- [2] C. Suryanarayana and A. Inoue, *Bulk Metallic Glasses* (CRC, Boca Raton, 2017).
- [3] D. V. Louzguine-Luzgin, V. Y. Zadorozhnyy, S. V. Ketov, Z. Wang, A. A. Tsarkov, and A. L. Greer, On room-temperature quasi-elastic mechanical behaviour of bulk metallic glasses, *Acta Mater.* **129**, 343 (2017).
- [4] T. C. Hufnagel, C. A. Schuh, and M. L. Falk, Deformation of metallic glasses: Recent developments in theory, simulations, and experiments, *Acta Mater.* **109**, 375 (2016).
- [5] F. Zhu, A. Hirata, P. Liu, S. Song, Y. Tian, J. Han, T. Fujita, and M. Chen, Correlation between Local Structure Order and Spatial Heterogeneity in a Metallic Glass, *Phys. Rev. Lett.* **119**, 215501 (2017).
- [6] W. H. Wang, The elastic properties, elastic models and elastic perspectives of metallic glasses, *Prog. Mater. Sci.* **57**, 487 (2012).
- [7] H. Lou, Z. Zeng, F. Zhang, S. Chen, P. Luo, X. Chen, Y. Ren, V. B. Prakapenka, C. Prescher, X. Zuo, T. Li, J. Wen, W. H. Wang, H. Sheng, and Q. Zeng, Two-way tuning of structural order in metallic glasses, *Nat. Commun.* **11**, 314 (2020).
- [8] X. Y. Wang, W. K. Wang, Z. J. Zhan, F. Y. Xu, N. Y. Zhang, F. X. Wang, Y. Chen, Y. T. Pang, L. P. Zhao, and J. Wang, Compression behaviour and micro-structure evaluation of $Zr_{57}Nb_5Cu_{15.4}Ni_{12.6}Al_{10}$ bulk metallic glass under high pressure, *Mater. Lett.* **61**, 2170 (2007).
- [9] G. Li, Y. C. Li, Q. Jing, T. Xu, L. Qi, M. Z. Ma, J. Liu, T. Zhang, and R. P. Liu, Atomic configuration evaluation of $Zr_{60}Ni_{21}Al$ bulk metallic glass under high pressure, *Mater. Chem. Phys.* **113**, 937 (2009).
- [10] N. Mattern, J. Bednarcik, H.-P. Liermann, and J. Eckert, Structural behaviour of $Pd_{40}Cu_{30}Ni_{10}P_{20}$ metallic glass under high pressure, *Intermetallics* **38**, 9 (2013).
- [11] M. Martin, T. Sekine, T. Kobayashi, L. Kecskes, and N. N. Thadhani, High-pressure equation of the state of a zirconium-based bulk metallic glass, *Metall. Mater. Trans. A* **38**, 2689 (2007).
- [12] H. W. Sheng, H. Z. Liu, Y. Q. Cheng, J. Wen, P. L. Lee, W. K. Luo, S. D. Shastri, and E. Ma, Polyamorphism in a metallic glass, *Nat. Mater.* **6**, 192 (2007).
- [13] Q. S. Zeng, Y. C. Li, C. M. Feng, P. Liermann, M. Somayazulu, G. Y. Shen, H. K. Mao, R. Yang, J. Liu, T. D. Hu, and J. Z. Jiang, Anomalous compression behavior in lanthanum/ cerium-based metallic glass under high pressure, *Proc. Natl. Acad. Sci. USA* **104**, 13565 (2007).
- [14] Q. S. Zeng, Y. Ding, W. L. Mao, W. Yang, S. V. Sinogeikin, J. Shu, H. K. Mao, and J. Z. Jiang, Origin of Pressure-Induced Polyamorphism in $Ce_{75}Al_{25}$ Metallic Glass, *Phys. Rev. Lett.* **104**, 105702 (2010).
- [15] W. Zhao, Y. Y. Wang, R. P. Liu, and G. Li, High compressibility of rare earth-based bulk metallic glasses, *Appl. Phys. Lett.* **102**, 031903 (2013).
- [16] L. Li, Q. Luo, R. Li, H. Zhao, K. W. Chapman, P. J. Chupas, L. Wang, and H. Liu, Polyamorphism in Yb-based metallic glass induced by pressure, *Sci. Rep.* **7**, 46762 (2017).
- [17] L. Li, L. Wang, R. Li, D. Qu, H. Zhao, K. W. Chapman, P. J. Chupas, and H. Liu, Pressure-induced polyamorphism in lanthanide-solute metallic glasses, *Phys. Status Solidi RRL* **11**, 1700078 (2017).
- [18] Y. Y. Wang, X. Dong, X. Song, X. P. Li, and G. Li, The effect of composition on pressure-induced polyamorphism in metallic glasses, *Mater. Lett.* **192**, 142 (2017).
- [19] P. Dziegielewski, J. Antonowicz, A. Pietnoczka, O. Mathon, S. Pascarelli, I. Kantor, T. Shinmei, and T. Irifune, Pressure-induced transformations in Ce-Al metallic glasses: The role of stiffness of interatomic pairs, *J. Alloys Compd.* **757**, 484 (2018).
- [20] M. Wu, H. Lou, J. S. Tse, H. Liu, Y. Pan, K. Takahama, T. Matsuoka, K. Shimizu, and J. Jiang, Pressure-induced polyamorphism in a main-group metallic glass, *Phys. Rev. B* **94**, 054201 (2016).
- [21] Q. Du, X.-J. Liu, Q. Zeng, H. Fan, H. Wang, Y. Wu, S.-W. Chen, and Z.-P. Lu, Polyamorphic transition in a transition metal based metallic glass under high pressure, *Phys. Rev. B* **99**, 014208 (2019).
- [22] H. B. Lou, Y. K. Fang, Q. S. Zeng, Y. H. Lu, X. D. Wang, Q. P. Cao, K. Yang, X. H. Yu, L. Zheng, Y. D. Zhao, W. S. Chu, T. D. Hu, Z. Y. Wu, R. Ahuja, and J. Z. Jiang, Pressure-induced amorphous-to-amorphous configuration change in Ca-Al metallic glasses, *Sci. Rep.* **2**, 376 (2012).
- [23] F. D. Murnaghan, The compressibility of media under extreme pressures, *Proc. Natl. Acad. Sci. USA* **30**, 244 (1944).
- [24] F. Birch, Finite elastic strain of cubic crystals, *Phys. Rev.* **71**, 809 (1947).
- [25] J. Antonowicz, A. Pietnoczka, G. A. Evangelakis, O. Mathon, I. Kantor, S. Pascarelli, A. Kartouzian, T. Shinmei, and T. Irifune, Atomic-level mechanism of elastic deformation in the Zr-Cu metallic glass, *Phys. Rev. B* **93**, 144115 (2016).
- [26] P. Dziegielewski, O. Mathon, I. Kantor, S. Pascarelli, T. Shinmei, T. Irifune, and J. Antonowicz, High pressure atomic structure of Zr-Cu metallic glass via EXAFS spectroscopy and molecular dynamics simulations, *High Press. Res.* **40**, 54 (2019).
- [27] O. J. Kwon, Y. C. Kim, K. B. Kim, Y. K. Lee, and E. Fleury, Formation of amorphous phase in the binary Cu-Zr alloy system, *Met. Mater. Int.* **12**, 207 (2006).
- [28] M.-B. Tang, D.-Q. Zhao, M.-X. Pan, and W.-h. Wang, Binary Cu-Zr bulk metallic glasses, *Chin. Phys. Lett.* **21**, 901 (2004).
- [29] X. Fu, G. Wang, Y. Wu, W. Song, C. H. Shek, Y. Zhang, J. Shen, and R. O. Ritchie, Compressive ductility and fracture resistance in CuZr-based shape-memory metallic-glass composites, *Int. J. Plast.* **128**, 102687 (2020).
- [30] A. Younes, P. Nnamchi, J. Medina, P. Pérez, V. M. Villapún, F. Badimuro, S. Kamnis, E. Jimenez-Melero, and S. González, Wear rate at RT and 100 °C and operating temperature range of microalloyed $Cu_{50}Zr_{50}$ shape memory alloy, *J. Alloys Compd.* **817**, 153330 (2020).
- [31] K.-W. Park, J.-i. Jang, M. Wakeda, Y. Shibutani, and J.-C. Lee, Atomic packing density and its influence on the properties of Cu-Zr amorphous alloys, *Scr. Mater.* **57**, 805 (2007).
- [32] J. Ding, Y.-Q. Cheng, and E. Ma, Full icosahedra dominate local order in $Cu_{64}Zr_{34}$ metallic glass and supercooled liquid, *Acta Mater.* **69**, 343 (2014).
- [33] N. Mattern, P. Jován, I. Kaban, S. Gruner, A. Elsner, V. Kokotin, H. Franz, B. Beuneu, and J. Eckert, Short-range order of Cu-Zr metallic glasses, *J. Alloys Compd.* **485**, 163 (2009).

- [34] N. Jakse and A. Pasturel, Local order and dynamic properties of liquid and undercooled $\text{Cu}_x\text{Zr}_{1-x}$ alloys by ab initio molecular dynamics, *Phys. Rev. B* **78**, 214204 (2008).
- [35] A. K. Soper, *Empirical Potential Structure Refinement-A User's Guide* (ISIS Rutherford Appleton Laboratory, Didcot, UK, 2006).
- [36] See Supplemental Material at <http://link.aps.org/supplemental/10.1103/PhysRevB.105.064203> for removing the Bragg spots on the 2D scattering patterns acquired at high pressure and optimizing the atomic density, structure factor, and PDF at different pressures using the iterative procedure.
- [37] E. Soignard, C. J. Benmore, and J. L. Yarger, A perforated diamond anvil cell for high-energy x-ray diffraction of liquids and amorphous solids at high pressure, *Rev. Sci. Instrum.* **81**, 035110 (2010).
- [38] J. Krogh-Moe, A method for converting experimental X-ray intensities to an absolute scale, *Acta Crystallogr.* **9**, 951 (1956).
- [39] N. Norman, The Fourier transformation method for normalizing intensities, *Acta Crystallogr.* **10**, 370 (1957).
- [40] D. Waasmaier and A. Kirfel, New analytical scattering-factor functions for free atoms and ions, *Acta Crystallogr., Sect. A: Found. Crystallogr.* **51**, 416 (1995).
- [41] V. H. Smith, A. J. Thakkar, and D. C. Chapman, A new analytic approximation to atomic incoherent X-ray scattering intensities, *Acta Crystallogr., Sect. A: Cryst. Phys., Diffr., Theor. Gen. Crystallogr.* **31**, 391 (1975).
- [42] Y. Waseda, *The Structure of Non-Crystalline Materials* (McGraw-Hill, New York, 1980).
- [43] R. Kaplow, S. L. Strong, and B. L. Averbach, Radial density functions for liquid mercury and lead, *Phys. Rev.* **138**, A1336 (1965).
- [44] J. H. Eggert, G. Weck, P. Loubeyre, and M. Mezouar, Quantitative structure factor and density measurements of high-pressure fluids in diamond anvil cells by x-ray diffraction: Argon and water, *Phys. Rev. B* **65**, 174105 (2002).
- [45] G. Sheng, V. B. Prakapenka, M. L. Rivers, and S. R. Sutton, Structural investigation of amorphous materials at high pressures using the diamond anvil cell, *Rev. Sci. Instrum.* **74**, 3021 (2003).
- [46] F. Decremps, G. Morard, G. Garbarino, and M. Casula, Polyamorphism of a Ce-based bulk metallic glass by high-pressure and high-temperature density measurements, *Phys. Rev. B* **93**, 054209 (2016).
- [47] G. Morard, G. Garbarino, D. Antonangeli, D. Andrault, N. Guignot, J. Siebert, M. Roberge, E. Boulard, A. Lincot, A. Denoed, and S. Petitgirard, Density measurements and structural properties of liquid and amorphous metals under high pressure, *High Press. Res.* **34**, 9 (2014).
- [48] M. N. Magomedov, The calculation of the parameters of the Mie-Lennard-Jones potential, *High Temp.* **44**, 513 (2006).
- [49] B. H. Toby and T. Egami, Accuracy of pair distribution function analysis applied to crystalline and non-crystalline materials, *Acta Crystallogr., Sect. A: Cryst. Phys., Diffr., Theor. Gen. Crystallogr.* **48**, 336 (1992).
- [50] G. S. Cargill III and F. Spaepen, Description of chemical ordering in amorphous alloys, *J. Non-Cryst. Solids* **43**, 91 (1981).
- [51] J. D. Bernal, Geometry of the structure of monatomic liquids, *Nature (London)* **185**, 68 (1960).
- [52] D. Ma, A. D. Stoica, X. L. Wang, Z. P. Lu, B. Clausen, and D. W. Brown, Elastic moduli inheritance and the weakest link in bulk metallic glasses, *Phys. Rev. Lett.* **108**, 085501 (2012).
- [53] D. B. Miracle, The efficient cluster packing model - An atomic structural model for metallic glasses, *Acta Mater.* **54**, 4317 (2006).